doi:10.20944/preprints202212.0356.v1

Article

Longitudinal Registration of Chest CT Images With Radiation-Induced Lung Disease

Fan-Ya Lin[1], Ya-Jing Li[1], Chi-En Lee[1], Kuo-Lung Lor[1], Hao-Jen Wang[1], Yeun-Chung Chang[2], and Chung-Ming Chen[1]*

[1] Institute of biomedical engineering, College of Medicine and College of Engineering, National Taiwan University, Taipei, Taiwan
[2] Department of Medical Imaging, National Taiwan University hospital, Taipei, Taiwan
* Correspondence: chung@ntu.edu.tw; Tel: +886-2-3366-5273

Abstract: Longitudinal image registration of pulmonary computed tomography (PCT) images may serve as an essential tool for investigating the relationship between radiation dose distribution and the occurrence and phenotype of radiation-induced lung disease (RILD). Although numerous longitudinal registration algorithms have been developed for PCT, most similarity-based approaches are not suitable for PCT involving RILD due to the complex tissue variation between two PCT images. Moreover, conventional feature-based approaches might fail to find a sufficient number of matched pairs of feature points due to the disparate lung deformation caused by breathing and RILD. To overcome the challenges resulting from RILD, component structure coherence point drift (CSCPD) was proposed to establish a deformation model by decomposing the chest into several components and matching them with individual parameters based on coherence point drift (CPD). Moreover, a regional vascular point matching (RVPM) algorithm was proposed to generate a vascular subtree and to substantially increase the number of corresponding pairs between two images. Eventually, the components were recomposed and aligned by a thin plate spline algorithm. A performance assessment on 15 pairs of PCT images of patients with RILD yielded recall and precision values of 0.85 and 0.89 for RVPM, respectively. Moreover, the target registration error of CSCPD with RVPM (2.3 ± 1.79) was significantly better than that of conventional CPD with RVPM (2.95 ± 1.89) and conventional CPD (5.04 ± 2.87). Therefore, the proposed registration system is robust to address the disparate deformation of lungs with RILD, and it improves registration accuracy within the parenchyma.

Keywords: Component Structure Coherence Point Drift; parenchyma change induced by radiotherapy; computed tomography; feature point sampling; regional vascular point matching; longitudinal registration

1. Introduction

For several years, radiotherapy (RT) has played an essential role in the treatment of thoracic malignancies such as lung adenocarcinoma, esophageal cancer, breast neoplasm, thymic epithelial neoplasm, malignant pleural mesothelioma, and lymphoma [1]. RT serves as a treatment of curative intent or an adjuvant treatment before surgery. However, radiation-induced lung disease (RILD) due to thoracic RT for non–small-cell lung cancer (NSCLC) is a common complication that leads to radiation pneumonitis (RP) and radiation fibrosis (RF), which can be fatal [2]. Moreover, the RT response varies among patients, and radiosensitivity depends on the tumor site. Therefore, evaluation of the relationship between the radiation dose distribution and the occurrence and phenotype of RILD is challenging in clinical settings. If the association can be observed intuitively and established into a model for quantifying the extent of injury caused by RILD, then doctors would be better equipped to alter treatment and doses for patients with NSCLC.

To establish the relationship between the radiation dose distribution and the occurrence and phenotype of RILD, longitudinal image registration is essential for aligning two pulmonary computed tomography (PCT) images in both space and time, enabling their comparison. However, the longitudinal registration of images of patients with RILD is difficult because of the complex tissue variation between PCT images. In the early phase, unusual PCT findings related to radiation toxicity include ground glass opacity (GGO) and lung consolidation; other abnormal diseases such as traction bronchiectasis, honeycombing, and scarring and obliteration of the alveolar air spaces may occur in the late phase [3–5]. Moreover, the disparate deformation of the lung caused by breathing may be observed [6]. As shown in Figure 1, comparison of lung images before RT (Figure 1 [a–c]) and after RT with RILD (Figure 1 [d–f]) revealed obvious differences. Therefore, adequate longitudinal PCT image registration is challenging.

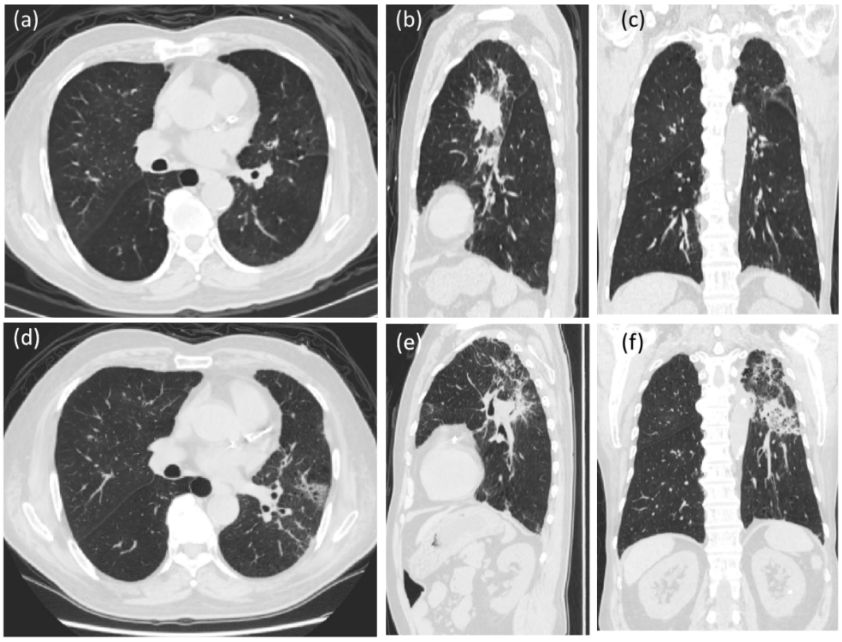

Figure 1. Lung (a–c) before RT and (d–f) after RT with RILD.

Generally, longitudinal image registration can be divided into two categories. The first category involves comparing two images and finding similarities. For example, optical flow involves adopting a gradient to establish the connection between source and target images [7], and it is usually applied to 4-dimensional computed tomography (4DCT) in lung imaging. In 2010, Song et al. [9] adopted diffeomorphism to establish transformation models and optimized registration results by using the image similarity metric and cross-correlation similarity metric, improving the assumption of intensity consistency between two lung images [10–12]. In 2015, Samavati et al. [22] proposed a hybrid deformable image registration algorithm consisting of a biomechanical model–based algorithm and an intensity-based algorithm. This algorithm improved on those proposed in previous studies and only considered the physiological aspect of respiratory motion by integrating a validated intensity-based method that was proposed by Glocker et al. [23] to refine the displacement, increasing registration accuracy in the entire image domain. In 2019, Castillo et al. [24] proposed a gradient-free quadratic penalty DIR (QPDIR) method to minimize both an image dissimilarity term, which is separable with respect to individual voxel displacements, and a regularization term derived from the classical leave-one-out cross-validation statistical method for maximizing the similarity between two PCT images. However, the aforementioned intensity-based image registration algorithms may be more suitable for PCT images of lungs with deformation caused by respiratory motion, because the intensity variation of PCT images with RILD is local and imperceptible for the global evaluation of similarity.

The second category of longitudinal image registration is feature-based image registration. This model consists of feature point description, matching, optimization, and deformation [25, 26]. This image registration algorithm specializes in feature extraction of not only image intensity but also anatomical information such as the shape, structure, and contour of an organ. Thus, they have better applicability in time-course studies. Therefore, feature-based image registration is more suitable for PCT images of patients with RILD to solve the problem of spatiotemporal deviation.

In the field of lung image registration, the structures of the trachea and pulmonary vessels are the most important features. For instance, Gorbunova et al. [27] extracted the centerlines of the pulmonary vessel tree and lung surfaces as geometrical features in intensity-based image registration. Martin et al. [28] used 3D scale invariant feature transform [29] to detect corner points as local descriptors and shape context [30] as global descriptors for shape matching. Previous studies on this topic have been conducted [31, 32]. The aforementioned methods have excellent performance in normal PCT images but may be inadequate for use in patients undergoing RT for NSCLC due to the substantial variation between images and damage of the structure of lung tissues. Therefore, an image registration algorithm that is flexible and robust to address the substantial image variation and disparate deformation of lungs is vital.

In contrast to the point-to-point registration approach, the point set registration approach that was proposed by Scott and Longuet-Higgins directly associates points [33]. However, its performance is poor for nonrigid objects. Another popular method for point set registration is iterative closest point (ICP) [34]. This method iteratively calculates the least square results of every closest corresponding point between two point sets to minimize the distance between each pair. However, ICP is unsuitable for our study due to the potential for large deviations when using the Euclidean distance to identify corresponding sets in cases with complex variations caused by RT. In contrast to ICP, coherent point drift (CPD) is a probabilistic method that assumes no specific point correspondence other than the one derived from the Euclidean distances between points. The corresponding point set is fit to Gaussian mixture models (GMMs). The Gaussian centroids of these models are used as the initialized points of the second set [8, 35]. Once the two point sets are optimally matched, the correspondence is the maximum GMM posterior probability. Moreover, CPD has the advantage of flexibility because most existing general-purpose rigid and nonrigid point-based registration schemes can be formulated using the CPD framework [36]. Therefore, CPD is more robust in terms of nonlinear deformation and noise. Several time-course studies have adopted CPD to align deformed lung images with shape variation in the trachea and pulmonary vessels [37–40]. However, conventional CPD applied to the entire thoracic cavity for image registration may not produce satisfactory results due to its inability to align the disparate deformations caused by breathing and to achieve local optimization. Furthermore, Hansen et al. [38, 41] also described that for the estimation of large deformations, CPD can be further improved. Therefore, the development of a modified CPD model for estimating complex tissue variation and deformation is necessary.

Generally, feature extraction of the lung parenchyma is challenging in the field of lung image registration because it shows up as a large dark region. Less corresponding pairs can be extracted from a dark region, thereby increasing the number of errors. Previous studies have used geometric information and the contrast between lung and surrounding tissues as feature descriptors [42]. In morphological methods, the trachea and bronchial tree were used as features of the structure of the lung parenchyma [43–45]. Moreover, gray-level thresholding and component analysis have been used to identify the boundaries and location of the lungs [46–50]. Our study was inspired by the aforementioned methods to address the challenge of image registration in patients with RILD.

This paper is organized as follows. Section 2 describes the unique idea of the proposed image registration algorithm and the details of processes as well as the design of the experiments for demonstrating the algorithm. Section 3 provides a summary of the experimental results, which demonstrated that the proposed image registration algorithm was able to align the clinical subjects and was an improvement relative to CPD. Finally, discussions and conclusions are drawn in Sections 4 and 5, respectively.

2. Materials and Methods

The proposed algorithm, namely the component structure CPD (CSCPD) algorithm, comprises segmentation, feature point extraction, and image registration. Its pipeline is displayed in Figure 2 and can be described as follows:

1. Generation of the component structure: the bones and organs, such as the ribs, sternum, vertebrae, trachea, lung, and pulmonary vessels, are segmented into several components.
2. Global prealignment: the roughly rigid registration of the vertebrae with slight deformations.
3. Surface sampling: the contours of the segmented components are extracted as feature points by the growing neural gas (GNG) method.
4. Component subtree generation and matching: In this study, the lungs have evident deformation and are affected by RILD. However, the feature points of the inner lung are insufficient. Therefore, we propose generating subtrees of the pulmonary vessels and matching their corresponding pairs using regional vascular point matching (RVPM).
5. CSCPD registration: every component is based on individual characteristics to be aligned by CPD.
6. Thin plate spline (TPS): a deformation model is established.

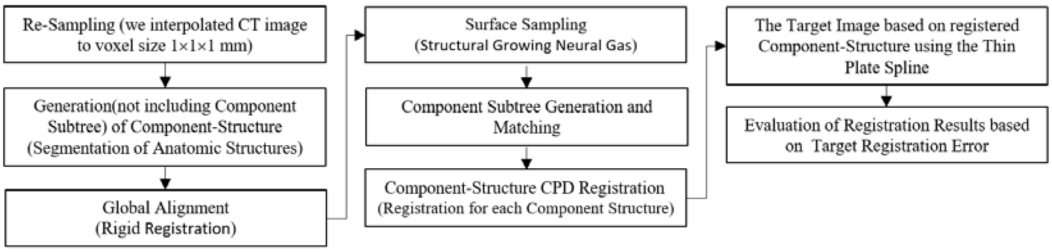

Figure 2. CSCPD algorithm.

2.1. Experiment Setup

The dataset is adopted from National Taiwan University hospital (NTUH), and these patients with non-small cell lung cancer (NSCLC) underwent the thoracic RT. The study is with the approval of the NTUH institutional review board and informed consent being waived. The thoracic CT scans of the NTUH dataset were retrospectively selected from 9845 NTUH patients with thoracic CT scans between April and November 2010.

2.2. Resampling

In this study, for the series of PCT images, linear interpolation was adopted to reconstruct 3D models with a voxel size of 1 × 1 × 1 mm.

2.3. Generation of Component Structure

2.3.1. Segmentation of Bones

In contrast to the lungs, the bones in the chest, such as the ribs, sternum, and vertebrae, are affected by radiation and have consistency of the anatomical structure. Therefore, the bones are extracted by adaptive thresholding [13], as shown in the left of

Figure 3. Each rib attached to a vertebra as one connected component must be separated from the corresponding vertebra. Lee [14] proposed the rib growing method to determine the boundaries between the ribs and vertebrae and to segment the outward portion of the ribs from the seed region, as shown in Figure 3 (a). Moreover, the sternum, as a plate-like structure, is segmented by the method proposed by Frangi et al. in 1998 [15]. Eventually, the vertebrae are obtained when the ribs and sternum are segmented. The segmentation results of the sternum and vertebrae are shown in Figures 3 (b) and (c). These bone tissues belong to the group CP_1 of CPD.

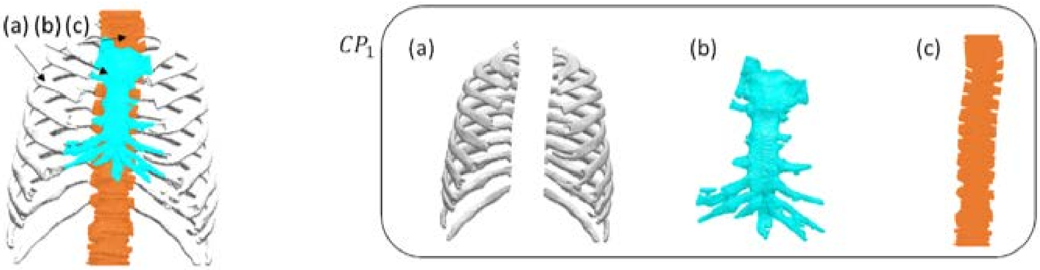

Figure 3. Segmentation of bones in chest. (a) Ribs, (b) sternum, and (c) vertebrae.

2.3.2. Segmentation of the Trachea

To extract the structure of the trachea, the region growing method was used to calculate the central line of the trachea. The potential structure of the trachea that is not exposed around the end points is searched by local disks. Each disk adopts first order derivatives to calculate the gradient direction of all pixels around the end points. The histogram of the gradient is subsequently computed, and the peak of the histogram is assigned as the dominant orientation of the disk, indicating that a more complete structure of the trachea has been obtained. The pipeline and the growing results are displayed in Figure 4. The trachea belongs to the group CP_2 of CPD.

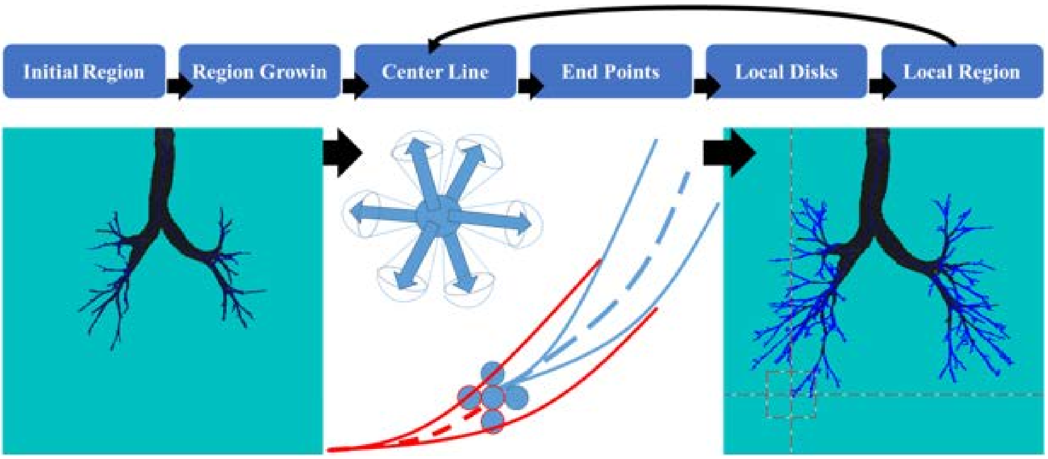

Figure 4. Segmentation of trachea. Region growing method was adopted to calculate initial structure of trachea, and potential structure was searched by local disks which used first order derivatives to calculate gradient direction around end points.

2.3.3. Segmentation of the Lung

In this study, the boundaries of the lung were divided into three major portions: the outer border (costal), the inner border (medial), and the bottom border (diaphragmatic). The outer and inner borders before the bottom border were calculated.

To find the outer and inner borders of the lung, an adaptive rolling ball algorithm was proposed by adjusting the size of a rolling ball to fit the boundaries. First, the corner points (green points) between the inner and outer lung surface were determined. A large rolling ball (orange circle) was adopted to find the inner border, and a small rolling ball was adopted to find the outer border, as shown in Figure 5 (a). The large rolling ball prevented oversegmentation and smoothed the border, which had a notch (marked by yellow arrow) caused by the segmentation of the trachea. The inner border was denoted by yellow and red lines, as shown in Figure 5 (b).

Eventually, the bottom border was composed by the lowest points of the lung. The results of the segmentation of the outer, inner, and bottom borders are shown in Figures 5 (c), (d), and (e), respectively. They belong to the groups CP_3, CP_4, and CP_5 of CPD, respectively.

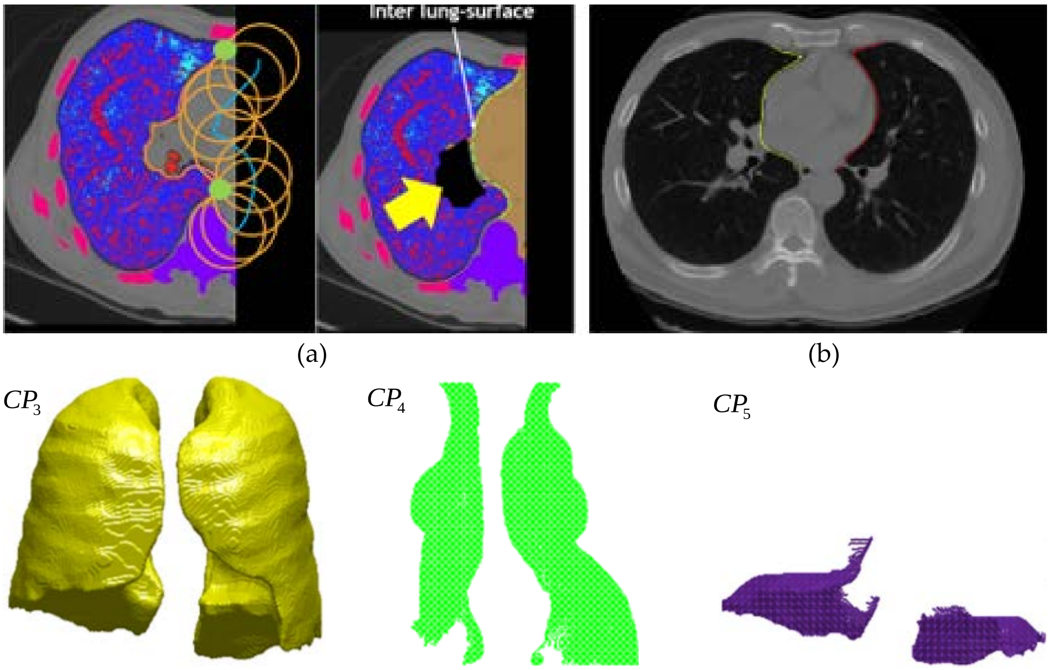

(a) (b)

(c) (d) (e)

Figure 5. Segmentation of the lung. (a) Adaptive rolling ball algorithm was used to find outer and inner borders of lung by adjusting size of rolling ball to fit boundaries. (b) Inner border was denoted by yellow and red lines. Segmentation results are comprised of (c) outer border, (d) inner border, and (e) bottom border.

2.3.4. Segmentation of Pulmonary Vessels

As shown in Section 2.3.1, the plate-like structure is segmented using the method proposed by Frangi et al. [15]. It can also be applied to tubular structures, such as the pulmonary vessels. λ_n indicates the eigenvalue of a Hessian matrix with the n-th smallest magnitude ($|\lambda_1| \le |\lambda_2| \le |\lambda_3|$), and a pixel belonging to a vessel region is signaled as $|\lambda_3| \cong |\lambda_2| \gg |\lambda_1|$. Then, the defined vesselness function is represented as follows:

$$\mathcal{V}_0(s) = \begin{cases} 0 & \text{if } \lambda_2 > 0 \text{ or } \lambda_3 > 0 \\ \left(1 - \exp\left(-\frac{\mathcal{R}_A^2}{2\alpha^2}\right)\right) \exp\left(-\frac{\mathcal{R}_B^2}{2\beta^2}\right) \left(1 - \exp\left(-\frac{\mathcal{S}^2}{2c^2}\right)\right) & \text{otherwise} \end{cases} \tag{1}$$

$$\mathcal{R}_A = \frac{|\lambda_2|}{|\lambda_3|} \tag{2}$$

$$\mathcal{R}_B = \frac{|\lambda_1|}{\sqrt{|\lambda_2 \lambda_3|}} \tag{3}$$

$$\mathcal{S} = \sqrt{\sum_{1 \le i \le 3} \lambda_i^2} \tag{4}$$

where α, β, and c are the thresholds that control the sensitivity of the line filter to the measures $\mathcal{R}_A$, $\mathcal{R}_B$, and $\mathcal{S}$. Through the vesselness function, the pulmonary vessels are extracted, as shown in Figure 6. They may be divided into several subportions based on their characteristics, and they belong to the groups $CP_6, \ldots, CP_N$ of CPD.

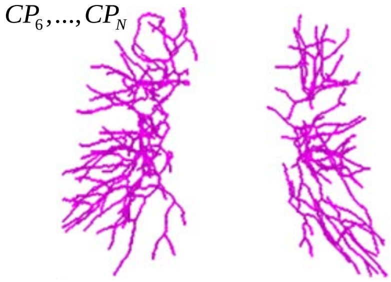

Figure 6. Segmentation of pulmonary vessels.

2.4. Global Prealignment of Two PCT Images

Because the vertebrae have slight deformation, rigid registration is suitable for global prealignment between two PCT images. The rigid transformation model can be decomposed into a linear transformation and a simple translation [16]. The rigid transformation function assumes that $f: V \rightarrow \mathrm{W}, \forall(x, y, z) \in \mathrm{V}, (x', y', z') \in \mathrm{W}$ and is mathematically expressed in the 3D formula as follows:

$$\begin{pmatrix} x' \\ y' \\ z' \end{pmatrix} = \begin{pmatrix} 1 & 0 & 0 \\ 0 & \cos(\theta_x) & -\sin(\theta_x) \\ 0 & \sin(\theta_x) & \cos(\theta_x) \end{pmatrix} \begin{pmatrix} \cos(\theta_y) & 0 & -\sin(\theta_y) \\ 0 & 1 & 0 \\ \sin(\theta_y) & 0 & \cos(\theta_y) \end{pmatrix}$$

$$\begin{pmatrix} \cos(\theta_z) & -\sin(\theta_z) & 0 \\ \sin(\theta_z) & \cos(\theta_z) & 0 \\ 0 & 0 & 1 \end{pmatrix} \begin{pmatrix} x \\ y \\ z \end{pmatrix} + \begin{pmatrix} dx \\ dy \\ dz \end{pmatrix} \tag{5}$$

The measure of match (MOM) algorithm proposed by Matsopoulos et al. [17] is used as the cost function to find the best solution and is represented as follows:

$$MOM = \frac{1}{N} \sum \sqrt{(x - x')^2 + (y - y')^2 + (z - z')^2}, \forall(x, y, z) \in \mathrm{V}, (x', y', z') \in \mathrm{W} \tag{6}$$

It is the average Euclidean distance between two PCT images. The simulated annealing method is adopted to optimize the best solution for the MOM algorithm [18].

2.5. Surface Sampling

After these components were segmented individually, the GNG method was adopted to extract a set of feature points for establishing the important topology of contours [19]. CP_k^t represents the *k*-th group of the component structure, and its feature point extraction can be calculated as follows:

$$GNG(CP_k^t), \ 1 \leq k \leq N \tag{7}$$

where t is the ordinal number for capturing PCT. When $k = 1$, CP_1^t comprises the ribs, sternum, and vertebrae; when $k = 2$, CP_2^t is the trachea; when $k = 3$, CP_3^t is costal; when $k = 4$, CP_4^t is medial; when $k = 5$, CP_5^t is diaphragmatic; when $6 \leq k \leq N$, $CP_6^t, \cdots, CP_N^t$ comprises the pulmonary vessels.

2.6. Component Subtree Generation and Matching

Conventional feature-based approaches can fail to find a sufficient number of feature points of the lung due to disparate deformation caused by breathing and RILD. To overcome this problem, the RVPM algorithm was proposed. The RVPM algorithm generates additional reliable feature points (named subtrees) from the branch points of pulmonary vessels and matches them using five conditions. Let u_i be the branch points of the first PCT image T_1, and $U_i = U(u_i)$ represents the volume of interest (VOI) with the center at u_i and radius = 25 voxels; v_m is the branch point of the second PCT image T_2, and $V_m = V(v_m)$ represents the VOI with the center at v_m and radius = 25 voxels. They are depicted in Figure 7.

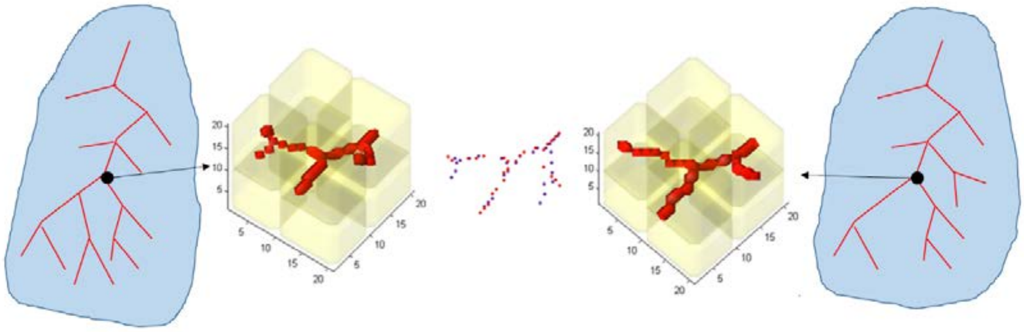

Figure 7. Corresponding pairs of branch points between PCT images T_1 and T_2 are evaluated by RVPM.

After global prealignment, the registered T_2 is expressed as $F^{rigid}(V_m)$, and the function of u_i and v_m is represented as follows:

$$\mathrm{MSOV}(u_i, v_m) = \left\{|u - u'| \middle| \forall u \in U_i, u'_i \in F^{rigid}\left(V(v_m)\right)\right\}. \tag{8}$$

Then, the corresponding pairs are determined using the following conditions:

1. The Euclidean distance between u_i and u'_i is related to the error of the rigid registration and is represented as follows:

$$\mathrm{CenterDist} = |u_i - u_i'|. \tag{9}$$

If the Euclidean distance is smaller, the branch points of u_i and v_m are more similar.

2. If the standard deviation of $\mathrm{MSOV}(u_i, v_m)$ is smaller, then the branch points of u_i and v_m are more similar.

3. The number of connected vessels at u_i and v_m is $NV(u_i)$ and $NV(v_m)$, respectively. If the difference between them, which can be expressed as $\Delta NV(u_i, v_m) = |NV(u_i) - NV(v_m)|$ is smaller, then the branch points of u_i and v_m are more similar.

4. The robust 3D tree registration proposed by Loeckx et al. [20] is adopted to evaluate the correspondence between u_i and v_m and is represented as follows:

$$P\left(C_{i,m}\right) = \sum_j \sum_l \frac{1}{\sqrt{2\pi\sigma^2}} \exp\left(-\frac{\left(\Phi_{i,j}^{T_1} - \Phi_{m,n}^{T_2}\right)^2}{\sigma^2}\right) = m_{G,im}, \tag{10}$$

where $\Phi_{i,j}^{T_1}$ is the difference of the Euclidean distance between u_i and neighboring branch points, and $\Phi_{m,n}^{T_2}$ is the difference of the Euclidean distance between v_m and neighboring branch points.

5. The difference of the radius of the vessel between u_i and v_m can be represented as follows:

$$\Delta VR(u_i, v_m) = |r(u_i) - r(v_m)| \tag{11}$$

If the distance is smaller, the branch points of u_i and v_m are more similar.

Eventually, the connected component is adopted to remove those tiny vessels, and the corresponding pairs of branch points between T_1 and T_2 are obtained using the aforementioned conditions. Furthermore, the subtrees are skeletonized and sampled for CSCPD. In the middle of Figure 7, the result of subtree matching is shown. The blue points represent the sampling of the subtree before RT and are matched with the red points, which represent the sampling of the subtree after RT.

2.7. Component Structure CPD Registration

After feature point extraction by GNG, the groups of components in the PCT images obtained at T_2 are individually registered to the corresponding groups in PCT images obtained at T_1 by CSCPD, which is expressed as follows:

$$(PS_k^1, PS_k^2) = CPD\big(GNG(CP_k^1), GNG(CP_k^2)\big),\ 1 \le k \le N \tag{12}$$

where PS_k^1, PS_k^2 are the registration results of the *k*-th group of components in the PCT images obtained at T_1 and T_2. Then, the registered results of components are combined into the PCT image of the entire chest, which is presented as follows:

$$PS^1 = \bigcup_{k=1}^{N} PS_k^1,\ 1 \le k \le N \tag{13}$$

$$PS^2 = \bigcup_{k=1}^{N} PS_k^2,\ 1 \le k \le N \tag{14}$$

where PS^1, PS^2 are the final registration results for all the bones and organs in the chest. These are used to evaluate the accuracy of the proposed image registration algorithm.

2.8. Thin Plate Spline

The nonlinear model based on TPS is employed to deform the nth PCT image to increase its similarity to the first PCT image [21]. The TPS model uses interpolation between these corresponding points based on the cubic spline function.

2.8. Evaluation Methods for RVPM and CSCPD

To evaluate the proposed RVPM algorithm, the accuracy of the results of subtree matching is calculated using a precision and recall method. The formula is as follows:

$$Recall = \frac{TP}{TP+FN} \tag{15}$$

$$Precision = \frac{TP}{TP+FP} \tag{16}$$

where *TP* is true positive, *FN* is false negative, and *FP* is false positive. Moreover, to evaluate the proposed CSCPD algorithm, the performance of the registration results is calculated based on target registration error (TRE), which adopts the results of *TP* and *FP* and is calculated as follows:

$$\mathrm{TRE} = \sqrt{(x_{t_i} - x_{l_i})^2 + (y_{t_i} - y_{l_i})^2 + (z_{t_i} - z_{l_i})^2} \tag{17}$$

where $(x_{t_i}, y_{t_i}, z_{t_i})$ and $(x_{l_i}, y_{l_i}, z_{l_i})$ are the *i*-th target feature point and the *i*-th estimated feature point, respectively.

3. Results

3.1. Evaluation of the RVPM Algorithm

The accuracy of RVPM was evaluated by precision and recall. In Table 1, the validations of the matching results from 15 subjects are shown. The precision and recall of the training data set are 0.89 and 0.85, respectively. Both the precision and recall of the testing data set are more than 0.8. Moreover, the area under the precision–recall curves is more than 0.9, which indicates that RVPM is extremely precise.

Table 1. Precision and recall results of RVPM.

Test Case NO.	Number of Matched Branch points		training		test		AUC of PR curve
	Left Lung	Right Lung	Recall	Precision	Recall	Precision	
1	106	89	0.85	0.89	0.82	0.92	0.94
2	86	69	0.85	0.89	0.80	0.93	0.91
3	96	72	0.85	0.89	0.95	0.89	0.97
4	112	89	0.85	0.89	0.88	0.83	0.92
5	100	80	0.85	0.89	0.86	0.89	0.93
6	92	81	0.85	0.89	0.80	0.93	0.93
7	90	150	0.85	0.90	0.82	0.92	0.95
8	130	54	0.85	0.90	0.83	0.88	0.92
9	50	114	0.85	0.89	0.97	0.92	0.98
10	36	130	0.85	0.89	0.85	0.94	0.94
11	101	115	0.85	0.89	0.82	0.89	0.91
12	118	58	0.85	0.89	0.81	0.93	0.94
13	125	160	0.85	0.89	0.93	0.91	0.97
14	121	94	0.85	0.89	0.94	0.84	0.97
15	45	59	0.85	0.89	0.80	0.87	0.90

3.2. Accuracy Comparison of Lung Image Registration Algorithms

TRE is adopted to evaluate the lung image registration results of CPD, CPD with RVPM, and CSCPD with RVPM. In Table 2, CSCPD with RVPM has the best performance, and the accuracy of CPD obviously increases after RVPM is used. Moreover, the *t*-test results ($P < 0.05$) between CSCPD and CPD reveal that accuracy is 0.001236 for the one-tail test and 0.002472 for the two-tailed test, which represents a significant difference. Therefore, RVPM significantly improves the registration results for the lung parenchyma, and CSCPD is useful for addressing the problem of the complex variation caused by RILD and disparate deformation.

Table 2. Accuracy comparison

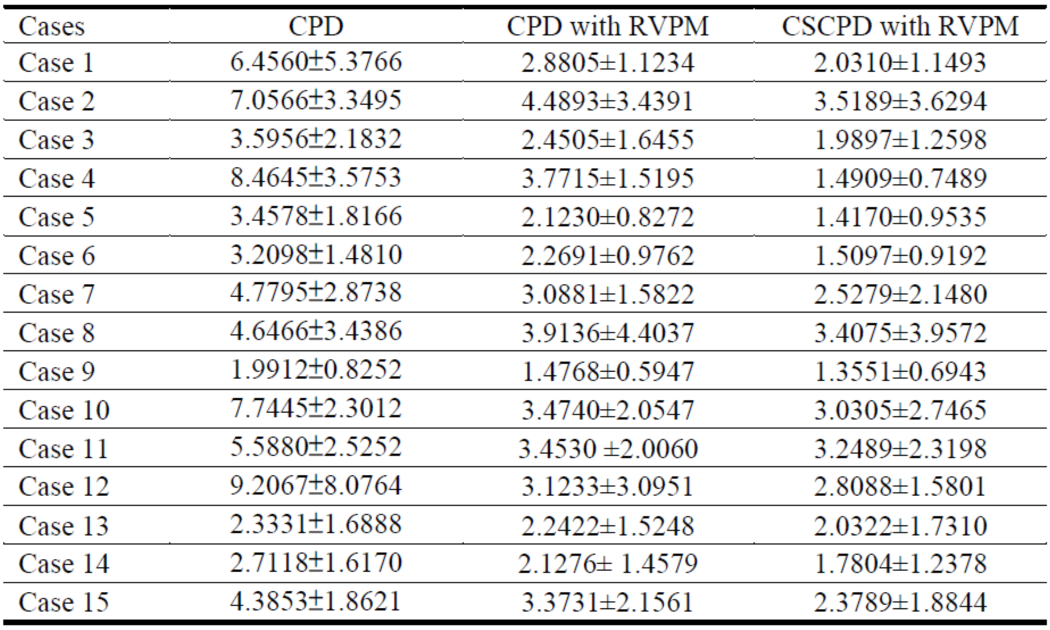

Cases	CPD	CPD with RVPM	CSCPD with RVPM
Case 1	6.4560±5.3766	2.8805±1.1234	2.0310±1.1493
Case 2	7.0566±3.3495	4.4893±3.4391	3.5189±3.6294
Case 3	3.5956±2.1832	2.4505±1.6455	1.9897±1.2598
Case 4	8.4645±3.5753	3.7715±1.5195	1.4909±0.7489
Case 5	3.4578±1.8166	2.1230±0.8272	1.4170±0.9535
Case 6	3.2098±1.4810	2.2691±0.9762	1.5097±0.9192
Case 7	4.7795±2.8738	3.0881±1.5822	2.5279±2.1480
Case 8	4.6466±3.4386	3.9136±4.4037	3.4075±3.9572
Case 9	1.9912±0.8252	1.4768±0.5947	1.3551±0.6943
Case 10	7.7445±2.3012	3.4740±2.0547	3.0305±2.7465
Case 11	5.5880±2.5252	3.4530 ±2.0060	3.2489±2.3198
Case 12	9.2067±8.0764	3.1233±3.0951	2.8088±1.5801
Case 13	2.3331±1.6888	2.2422±1.5248	2.0322±1.7310
Case 14	2.7118±1.6170	2.1276± 1.4579	1.7804±1.2378
Case 15	4.3853±1.8621	3.3731±2.1561	2.3789±1.8844

3.3. Registration Results of CSCPD in the Chest

In addition to the lung, the organs and bones in the chest are modeled as several components for aligning by CSCPD. The components consist of the (a) bones (ribs, vertebrae, and sternum), (b) trachea, (c and d) medial surface, and (e) diaphragmatic surface, and the results of feature point set matching are displayed in Figure 8. The red points are the feature point sets before RT, and the blue points are the feature point sets after RT. Moreover, the left feature point sets in every subfigure are not aligned by CSCPD and have obvious deviations and contour variation relating to the effects of respiratory motion and RT. After image registration by CSCPD, the right feature point sets in every subfigure are well aligned (most feature point sets are matched).

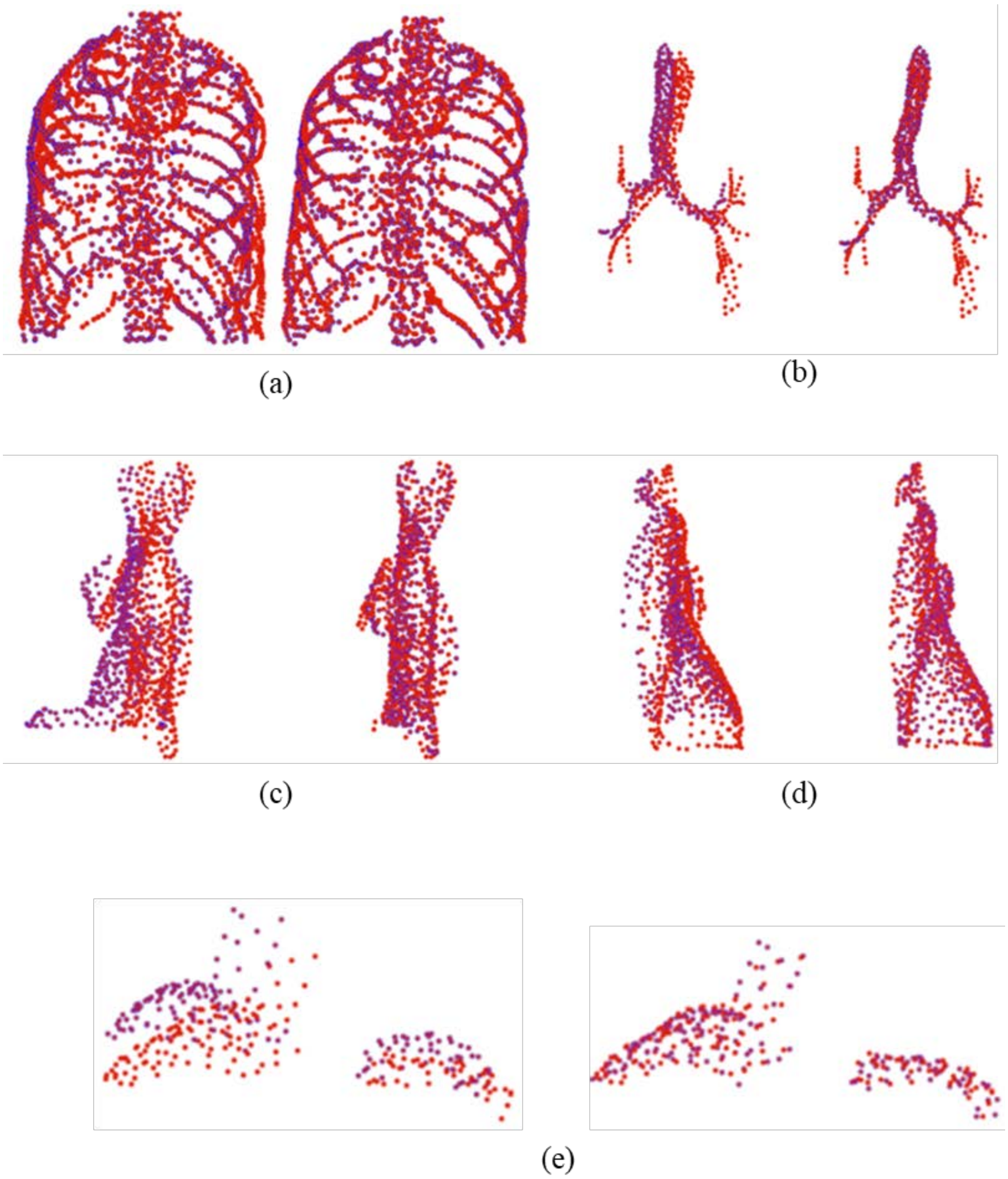

Figure 8. Feature point sets matched by CSCPD. Components consist of (a) bones (ribs, vertebrae, and sternum) with 1400 feature points, (b) trachea with 300 feature points, (c) left medial surface with 500 feature points, (d) right medial surface with 500 feature points, and (e) diaphragmatic surface with 150 feature points. Red points are feature point sets before RT and blue points are feature point sets after RT. After left feature point sets are registered by CSCPD, right feature point sets in every subfigure are well aligned.

4. Discussion

To obtain a better understanding of the registration results of CSCPD and CPD in PCT images, images in the axial view, sagittal plane, and coronal plane were compared, as shown in Figure 9. CPD registration results are displayed in Figure 9 (a–c), and CSCPD registration results are shown in Figure 9 (d–f). Post-RT PCT images are colored purple, pre-RT images are green, and the gray portions are the overlay. The larger gray portions in CSCPD implies the better aligning performance of CSCPD. Comparison of the details in the subfigures revealed the following: in the axial view, the heartbeat, denoted by white arrows, causes disparate deformation and affects the registration results of the border of the medial surface; CSCPD is better able to match these points. In the sagittal plane, the respiratory motion, denoted by brown arrows, causes obviously disparate deformation and affects the registration results of the diaphragmatic surface; CSCPD is robust to address disparate deformation and provides better matching results. In the coronal plane, the portions of the bones and the costal surface of the lung are denoted by yellow arrows, and CSCPD also has a better performance, regardless of whether the deformation is nonrigid or rigid. Eventually, the tissue variation caused by RILD is denoted by blue arrows, and CSCPD is still better than CPD. This finding demonstrates that CSCPD is robust to address complex tissue variation and disparate deformation.

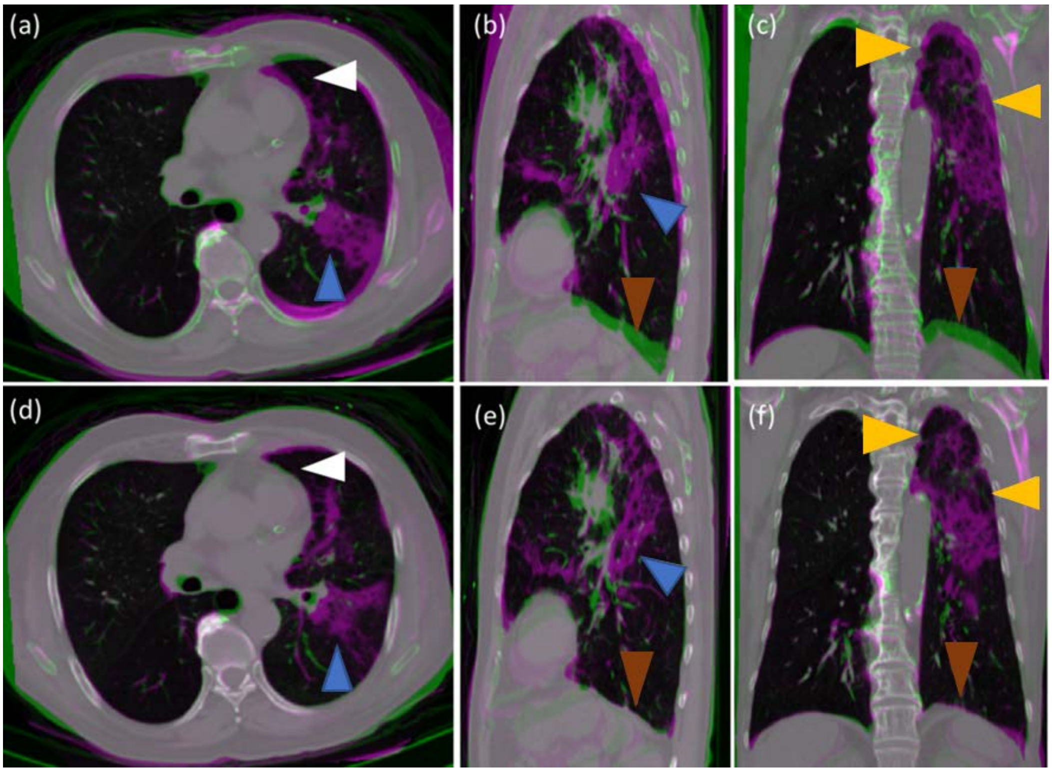

Figure 9. Registration results of CSCPD and CPD in PCT images. CPD registration results are displayed in the upper half, and CSCPD registration results are displayed in the lower half. Post-RT PCT images are purple, pre-RT images are green, and gray portions are overlay. In the axial view, (a) and (d), heartbeat, denoted by white arrows, causes disparate deformation. In the sagittal plane, (b) and (e), respiratory motion, denoted by brown arrows, causes obviously disparate deformation. In the coronal plane, (c) and (f), portions of the bones and costal surface of the lung are denoted by yellow arrows, and CSCPD has better performance, regardless of whether deformation is nonrigid or rigid. Tissue variation caused by RILD is denoted by blue arrows, and CSCPD is still better than CPD.

5. Conclusions

RILD due to thoracic RT for NSCLC is a common complication that leads to RP and RF. RP and RF are caused by radiation toxicity and can lead to unusual PCT findings such as GGO, lung consolidation, traction bronchiectasis, honeycombing, and scarring and obliteration of the alveolar air spaces. A longitudinal PCT image registration algorithm is an essential tool for investigating the relationship between the radiation dose distribution and the occurrence and phenotype of RILD. However, the longitudinal registration of images of patients with RILD is difficult because of the complex tissue variation and disparate deformation of the lung tissue. Conventional feature-based approaches might fail to find a sufficient number of matched pairs of feature points to account for the disparate deformation caused by breathing and RILD. Moreover, feature extraction of the lung parenchyma is a challenging problem because it shows up as a large dark region. Less corresponding pairs can be extracted from a dark region, thereby increasing the number of errors.

In this study, the CSCPD algorithm was proposed to address the problem of complex deformation. The unique idea of the algorithm is to establish a disparate deformation model by decomposing the chest into several components and matching them with individual parameters through nonrigid or rigid CPD. Moreover, the lung RVPM algorithm was proposed to generate the vascular subtree and substantially increase the corresponding pairs between the two images of lung parenchyma.

The demonstration experiments are based on 15 pairs of PCT images of patients with RILD. When evaluating the RVPM algorithm, the recall and precision of RVPM were 0.85 and 0.89, respectively. Moreover, a comparison of the accuracy of CSCPD with RVPM, CPD with RVPM, and CPD in lung image registration revealed that the TRE of CSCPD with RVPM (2.3 ± 1.79) was significantly better than that of conventional CPD with RVPM (2.95 ± 1.89) and conventional CPD (5.04 ± 2.87), indicating that RVPM significantly improves registration results for the lung parenchyma. Furthermore, comparison of the registration results between CSCPD and CPD in PCT images of the entire chest revealed that CSCPD has better performance, irrespective of whether the deformation is nonrigid or rigid. Therefore, the proposed registration system is robust to address the complex deformation of lungs with RILD and improves registration accuracy within the parenchyma.

Author Contributions: Fan-Ya Lin, Ya-Jing Li, Chi-En Lee, Yeun-Chung Chang and Chung-Ming Chen conceived and designed the experiments. Kuo-Lung Lor and Hao-Jen Wang conducted the experiments and collected data. Fan-Ya Lin, Ya-Jing Li and Chi-En Lee analyzed and interpreted data. Fan-Ya Lin and Chi-En Lee wrote the manuscript. All authors have read and agreed to the published version of the manuscript.

Funding: This work was supported in part by Ministry of Science and Technology of Taiwan under MOST Grants: MOST107-2221-E-002–074-MY3

Institutional Review Board Statement: The work was approved by the NTUH institutional review board.

Informed Consent Statement: The informed consent was waived.
Data Availability Statement: The dataset is adopted from National Taiwan University hospital (NTUH), and these patients with non-small cell lung cancer (NSCLC) underwent the thoracic RT.

Conflicts of Interest: The authors declare that they have no conflict of interest, financial or otherwise, to declare.

References

1. Arrieta, Oscar, et al. "National consensus of diagnosis and treatment of non-small cell lung cancer." *Revista de investigacion clinica; organo del Hospital de Enfermedades de la Nutricion* 65 (2013): S5-84.
2. Huang, Kitty, David A. Palma, and IASLC Advanced Radiation Technology Committee. "Follow-up of patients after stereotactic radiation for lung cancer: a primer for the nonradiation oncologist." *Journal of Thoracic Oncology* 10.3 (2015): 412-419.
3. Ghaye, B., Marie Wanet, and M. El Hajjam. "Imaging after radiation therapy of thoracic tumors." *Diagnostic and interventional imaging* 97.10 (2016): 1037-1052.
4. Davis, Sheila D., David F. Yankelevitz, and Claudia I. Henschke. "Radiation effects on the lung: clinical features, pathology, and imaging findings." *American journal of roentgenology (1976)* 159.6 (1992): 1157-1164.
5. Benveniste, M. F. K., et al. "New era of radiotherapy: an update in radiation-induced lung disease." *Clinical radiology* 68.6 (2013): e275-e290.
6. Christensen, Gary E., et al. "Tracking lung tissue motion and expansion/compression with inverse consistent image registration and spirometry." *Medical physics* 34.6Part1 (2007): 2155-2163.
7. Lefébure, Martin, and Laurent D. Cohen. "Image registration, optical flow and local rigidity." *Journal of Mathematical Imaging and Vision* 14.2 (2001): 131-147.
8. Myronenko, Andriy, and Xubo Song. "Point set registration: Coherent point drift." *IEEE transactions on pattern analysis and machine intelligence* 32.12 (2010): 2262-2275.

9. Song, Gang, et al. "Lung CT image registration using diffeomorphic transformation models." *Medical image analysis for the clinic: a grand challenge* (2010): 23-32.
10. Guerrero, Thomas, et al. "Reduction of pulmonary compliance found with high-resolution computed tomography in irradiated mice." *International Journal of Radiation Oncology* Biology* Physics* 67.3 (2007): 879-887.
11. Dawood, Mohammad, et al. "Respiratory motion correction in 3-D PET data with advanced optical flow algorithms." *IEEE transactions on medical imaging* 27.8 (2008): 1164-1175.
12. Castillo E, Castillo R, Zhang Y, Guerrero T. "Compressible image registration for thoracic computed tomography images." *J Med Biol Eng* (2009): 222–33.
13. Zhang, Jing, et al. "Fast segmentation of bone in CT images using 3D adaptive thresholding." *Computers in biology and medicine* 40.2 (2010): 231-236.
14. Lee, Jaesung, and Anthony P. Reeves. "Segmentation of individual ribs from low-dose chest CT." *Medical Imaging 2010: Computer-Aided Diagnosis*. Vol. 7624. SPIE, 2010.
15. Frangi, Alejandro F., et al. "Multiscale vessel enhancement filtering." *International conference on medical image computing and computer-assisted intervention*. Springer, Berlin, Heidelberg, 1998.
16. Van den Elsen, Petra A., E-JD Pol, and Max A. Viergever. "Medical image matching-a review with classification." *IEEE Engineering in Medicine and Biology Magazine* 12.1 (1993): 26-39.
17. Matsopoulos, George K., et al. "CT-MRI automatic surface-based registration schemes combining global and local optimization techniques." *Technology and Health Care* 11.4 (2003): 219-232.
18. Ingber, Lester. "Simulated annealing: Practice versus theory." *Mathematical and computer modelling* 18.11 (1993): 29-57.
19. Fritzke, Bernd. "A growing neural gas network learns topologies." *Advances in neural information processing systems* 7 (1994).
20. Loeckx, Dirk, et al. "3D lung registration using splineMIRIT and robust tree registration (RTR)." *Grand Challenges in Medical Image Analysis* (2010).
21. Bookstein, Fred L. "Principal warps: Thin-plate splines and the decomposition of deformations." *IEEE Transactions on pattern analysis and machine intelligence* 11.6 (1989): 567-585.
22. Samavati, Navid, Michael Velec, and Kristy Brock. "A hybrid biomechanical intensity based deformable image registration of lung 4DCT." *Physics in Medicine & Biology* 60.8 (2015): 3359.
23. Glocker, Ben, et al. "Dense image registration through MRFs and efficient linear programming." *Medical image analysis* 12.6 (2008): 731-741.
24. Castillo, Edward. "Quadratic penalty method for intensity-based deformable image registration and 4DCT lung motion recovery." *Medical physics* 46.5 (2019): 2194-2203.
25. Guan, Shao-Ya, et al. "A review of point feature based medical image registration." *Chinese Journal of Mechanical Engineering* 31.1 (2018): 1-16.
26. Boda, Somaraju. *Feature-based image registration*. Diss. 2009.
27. Gorbunova, Vladlena, et al. "Lung CT registration combining intensity, curves and surfaces." *2010 IEEE International Symposium on Biomedical Imaging: From Nano to Macro*. IEEE, 2010.
28. Urschler, Martin, et al. "SIFT and shape context for feature-based nonlinear registration of thoracic CT images." *International Workshop on Computer Vision Approaches to Medical Image Analysis*. Springer, Berlin, Heidelberg, 2006.
29. Cheung, Warren, and Ghassan Hamarneh. "N-sift: N-dimensional scale invariant feature transform for matching medical images." *2007 4th IEEE international symposium on biomedical imaging: from nano to macro*. IEEE, 2007.
30. Belongie, Serge, Jitendra Malik, and Jan Puzicha. "Shape context: A new descriptor for shape matching and object recognition." *Advances in neural information processing systems* 13 (2000).
31. Chui, Haili, and Anand Rangarajan. "A new algorithm for non-rigid point matching." *Proceedings IEEE Conference on Computer Vision and Pattern Recognition. CVPR 2000 (Cat. No. PR00662)*. Vol. 2. IEEE, 2000.
32. Gold, Steven, et al. "New algorithms for 2D and 3D point matching: pose estimation and correspondence." *Pattern recognition* 31.8 (1998): 1019-1031.
33. Scott, Guy L., and Hugh Christopher Longuet-Higgins. "An algorithm for associating the features of two images." *Proceedings of the Royal Society of London. Series B: Biological Sciences* 244.1309 (1991): 21-26.
34. Besl, Paul J., and Neil D. McKay. "Method for registration of 3-D shapes." *Sensor fusion IV: control paradigms and data structures*. Vol. 1611. Spie, 1992.
35. Myronenko, Andriy, Xubo Song, and Miguel Carreira-Perpinan. "Non-rigid point set registration: Coherent point drift." *Advances in neural information processing systems* 19 (2006).
36. Hu, Yipeng, et al. "Deformable vessel-based registration using landmark-guided coherent point drift." *International Workshop on Medical Imaging and Virtual Reality*. Springer, Berlin, Heidelberg, 2010.
37. Rao, Fan, Wen-long Li, and Zhou-ping Yin. "Non-rigid point cloud registration based lung motion estimation using tangent-plane distance." *Plos one* 13.9 (2018): e0204492.
38. Hansen, Lasse, Doris Dittmer, and Mattias P. Heinrich. "Learning deformable point set registration with regularized dynamic graph cnns for large lung motion in copd patients." *International Workshop on Graph Learning in Medical Imaging*. Springer, Cham, 2019.
39. Zhang, Jiayi, et al. "A 2D/3D non-rigid registration method for lung images based on a non-linear correlation between displacement vectors and similarity measures." *Journal of Medical and Biological Engineering* 41.3 (2021): 331-342.

doi:10.20944/preprints202212.0356.v1

---

40. Xia, Wei, and Xin Gao. "A fast deformable registration method for 4D lung CT in hybrid framework." *International journal of computer assisted radiology and surgery* 9.4 (2014): 523-533.
41. Hansen, Lasse, and Mattias P. Heinrich. "Deep learning based geometric registration for medical images: How accurate can we get without visual features?." *International Conference on Information Processing in Medical Imaging*. Springer, Cham, 2021.
42. Sluimer, Ingrid, et al. "Computer analysis of computed tomography scans of the lung: a survey." *IEEE transactions on medical imaging* 25.4 (2006): 385-405.
43. Lai-Fook, Stephen J. "Elasticity analysis of lung deformation problems." *Annals of biomedical engineering* 9.5 (1981): 451-462.
44. Tai, Ronald C., and George C. Lee. "Isotropy and homogeneity of lung tissue deformation." *Journal of Biomechanics* 14.4 (1981): 243-252.
45. Lai-Fook, STEPHEN J., and MICHAEL J. Kallok. "Bronchial-arterial interdependence in isolated dog lung." *Journal of Applied Physiology* 52.4 (1982): 1000-1007.
46. Armato III, Samuel G., and William F. Sensakovic. "Automated lung segmentation for thoracic CT: impact on computer-aided diagnosis1." *Academic Radiology* 11.9 (2004): 1011-1021.
47. Brown, Matthew S., et al. "Method for segmenting chest CT image data using an anatomical model: preliminary results." *IEEE transactions on medical imaging* 16.6 (1997): 828-839.
48. Hu, Shiying, Eric A. Hoffman, and Joseph M. Reinhardt. "Automatic lung segmentation for accurate quantitation of volumetric X-ray CT images." *IEEE transactions on medical imaging* 20.6 (2001): 490-498.
49. da Silva, Augusto Ferreira, et al. "Fast pulmonary contour extraction in X-ray CT images: a methodology and quality assessment." *Medical Imaging 2001: Physiology and Function from Multidimensional Images*. Vol. 4321. SPIE, 2001.
50. Zheng, Bin, et al. "A simple method for automated lung segmentation in X-ray CT images." *Medical Imaging 2003: Image Processing*. Vol. 5032. SPIE, 2003.